THE JOURNAL OF PHYSICAL CHEMISTRY C

pubs.acs.org/JPCC

Article

Microscopic Link between Electron Localization and Chemical Expansion in $AMnO_3$ and $ATiO_3$ Perovskites (A = Ca, Sr, Ba)

Astrid Marthinsen, Tor Grande, and Sverre M. Selbach*

Cite This: *J. Phys. Chem. C* 2020, 124, 12922−12932

Read Online

ACCESS | Metrics & More | Article Recommendations | Supporting Information

ABSTRACT: The microscopic origin of chemical expansion in perovskite oxides, due to formation of oxygen vacancies accompanied by formal reduction of a 3d transition metal, is studied by first-principles calculations. We compare the II−IV manganite and titanate series, having Ca, Sr, or Ba on the A site. In particular, the effect of electron localization is elucidated by systematically varying the Hubbard *U*, and we find that the localization behavior is significantly different in the manganites and titanates. The chemical expansion is explicitly calculated for all compounds, and we demonstrate that increasing on-site repulsion (Hubbard *U*) on the B site in the lattice yields increased chemical expansion in the manganites and reduced chemical expansion in the titanates. The opposite behavior of the manganites and titanates arises from different electrostatic screenings of oxygen vacancies. We show that this can be attributed to differences in electronic energy levels, specifically that Mn−O bonds are more covalent than Ti−O bonds. Fundamental understanding of electronic and crystal chemical origins of the important phenomenon of chemical expansion is required for rational design of oxide materials for energy technology, sensors, and actuators. We hope our analysis will inspire further fundamental studies of other oxides for solid state ionics applications.

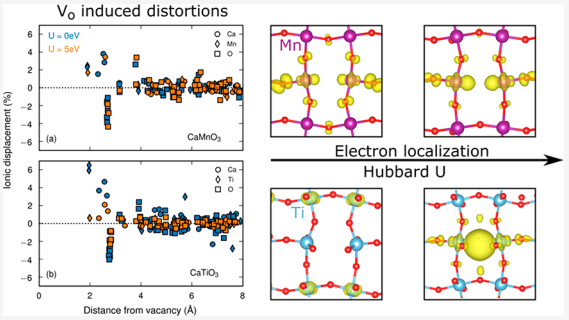

INTRODUCTION

Ever since Stuart Adler introduced chemical expansion as a term for a physical phenomenon in electroceramics in 2001,[1] there have been many efforts[2−4] to provide an understanding of the underlying microscopic mechanisms. Chemical expansion is defined as the spatial dilation of a material upon compositional changes, e.g., point defects such as cation or oxygen vacancies or interstitials. Stoichiometric expansion ϵ (in one dimension) resulting from a compositional change, δ, is given by

$$\epsilon = \frac{a - a_0}{a_0} = \alpha_C \delta \quad (1)$$

where a_0 is the initial lattice parameter, a is the resulting lattice parameter after dilution, and α_C is the chemical expansion coefficient, assuming linear behavior. Particularly in applications based on ionic conductivity, i.e., solid oxide fuel cells[5] or battery electrodes,[6] chemical expansion can lead to large mechanical stresses and ultimately cause device deterioration or failure.[7,8] Oxygen vacancies have attracted particular attention, being unavoidable in transition metal oxide ceramics at finite temperatures, and tunable by controlling the oxygen partial pressure. Chemical expansion by formation of oxygen vacancies can also serve as a route to new functionalities, e.g., making electrochemical actuators,[9] or serve as a strain mediation mechanism under tensile epitaxial strain in thin films.[10−12] Understanding the mechanisms driving chemical expansion is therefore highly important for the selection or design of new materials for various electrochemical applications.

The important degree of electron localization, i.e., the size of polarons forming around the vacancy, has been theoretically studied for CeO_{2-x} and $BaCeO_{3-x}$,[2] where increased localization of charge compensating electrons in Ce 4f states result in a large increase in the chemical expansion coefficient. The degree of chemical expansion is, however, a complex issue, depending on many underlying factors that are not fully understood, including crystal structure, chemical composition, and the presence of magnetic cations.[4] Specifically, transition metal oxides are expected to display more complex mechanisms for chemical expansion as d-electrons are much less localized than strongly localized f-electrons. Fluorites tend for example to display larger chemical expansion than perovskites,[7] which has been attributed to a larger change of the cation radii in fluorites than in perovskites.[4] Chemical expansion due to oxygen nonstoichiometry has been explored in various perovskite-structured materials, particularly materials

Received: March 8, 2020
Revised: May 14, 2020
Published: May 14, 2020

with potential for solid oxide fuel cells[13] and oxygen permeable membrane applications, including mixed-valent ferrites,[14,15] cobaltites, and solid solutions thereof,[16−21] as well as chromites.[22] Only small variations in chemical expansion were found with varying Co/Fe ratio in solid solutions of $La_{0.6}Sr_{0.4}Co_{1-y}Fe_yO_{3-\delta}$,[19] while the chemical expansion decreased with increasing Ni/Ga ratio in $La_{0.9}Sr_{0.1}Ga_{1-x}Ni_xO_{3-\delta}$.[23] Symmetry-dependent anisotropy was found in cation deficient $La_xSr_{1-x}MnO_{3+\delta}$ with the centrosymmetric rhombohedral $R\bar{3}c$ space group.[24] Upon oxidation, the effective tolerance factor becomes closer to unity as the B cation radius is reduced. This leads to a stronger contraction along the elongated *a*-axis than along the *c*-axis. The opposite anisotropic behavior was seen in cation deficient $BiFe_{1-x}Mn_xO_{3+\delta}$ within the *polar* rhombohedral *R*3*c* space group.[25,26] As the *c*-axis is more elongated than the *a*-axis, this results in stronger anisotropic chemical contraction along the former. Anisotropic chemical expansion upon oxygen deficiency has furthermore been reported in $La_{1-x}Sr_xCoO_{3-\delta}$[27] and $La_{1-x}Sr_xFeO_{3-\delta}$,[28] showing a significantly stronger expansion along the more compressed *c*-axis than along the *a*-axis. Oxygen and cation vacancies thus serve as an internal lattice strain mitigation mechanism.

This work focuses on the chemical expansion upon oxygen vacancy formation in the II−IV perovskite manganites and titanates with Ca, Sr, or Ba on the A site. The II−IV perovskite manganites gained particular attention after the discovery of colossal magnetoresistance in mixed valent manganites[29] and are also considered potential candidates for multiferroics.[11,30−32] Within the considered $AMnO_3$ series, $CaMnO_3$, with tolerance factor t = 0.977, attains a *Pbnm* crystal structure.[33] $SrMnO_3$ (t = 1.033) lies on the stability edge between a 4H hexagonal polytype and the perovskite structure,[34] and in the perovskite structure it is theoretically predicted to attain small rotational distortions from the aristotype, where the $R\bar{3}c$ and *Pbnm* are energetically degenerate.[11] $BaMnO_3$ (t = 1.097) attains a hexagonal 2H structure in its thermodynamic ground state, and it is not yet experimentally realized as perovskite. However, theoretically, perovskite $BaMnO_3$ is predicted to have a polar *Amm*2 ground state if the magnetic order is restricted to G-AFM.[31] Oxygen vacancies can have a large impact on the properties in the manganites, including induced large magnetoresistance in $CaMnO_{3-x}$,[35] and stabilization of cubic $SrMnO_{3-x}$ over the hexagonal polytype.[34] Oxygen vacancy formation has been explored in epitaxially strained manganites,[10−12,30] where the reverse effect of chemical expansion has been demonstrated: expansion of the crystal lattice lowers the formation energy of oxygen vacancies.

The II−IV titanates with Ca, Sr, and Ba on the A site have a systematically lower tolerance factor than the manganites due to the larger Shannon radii of Ti^{4+} (electronic configuration d^0) cations compared to that of Mn^{4+} ($t_{2g}^3e_g^0$), giving rise to more spatially extended d orbitals in the titanates. $CaTiO_3$ (t = 0.946) attains a *Pbnm* structure in its ground state,[36] and $SrTiO_3$ (t = 1.001) is in the *I*4/*mcm* space group in its ground state,[37] whereas the ground state structure of $BaTiO_3$ (t = 1.063) is the polar *R*3*m* space group.[38] Oxygen vacancies can also have a large impact on properties in the titanates. In $SrTiO_3$ oxygen vacancies have been reported to induce an insulator to metal transition,[39] superconductivity at low T and high carrier concentration[40] and alter the optical properties.[41] $BaTiO_3$ also exhibits an oxygen vacancy-induced insulator to metal transition, and interestingly retains its polar structure.[42]

Here we use density functional theory (DFT) calculations to compare the chemical expansions in titanates and manganites. The effects of orbital spatial extension, i.e., the structural impact of having localized versus delocalized charge compensating electrons, and the importance of electron localization by varying Hubbard U on the B site cation are investigated. We find that the localization behavior is opposite in the manganites and titanates with higher degree of electron localization leading to an increase in chemical expansion in the manganites and a reduction in the titanates. This is attributed to the large differences in electrostatic screening of the oxygen vacancy due to differences in electronic energy levels between Mn^{4+} and Ti^{4+}, and different degrees of covalency between Mn−O and Ti−O bonds.

COMPUTATIONAL DETAILS

Density functional theory (DFT) calculations were performed using the Vienna *ab initio* simulation package (VASP)[43−46] with projector-augmented wave (PAW)[47] potentials treating Ca(3p,4s), Sr(4s,4p,5s), Ba(5s,4p,6s), Mn(3p,3d,4s), Ti(3p,3d,4s), and O(2s,2p) as valence electrons. Calculations were performed with the PBEsol[48] functional and plane waves were expanded up to cutoff energy of 650 eV. To model the structural distortions caused by formation of a neutral oxygen vacancy, a 120-atom hexagonal supercell was used, with an oxygen vacancy (V_O) concentration of 1.38%. Initial testing with $BaTiO_3$ using larger supercells (3 × 3 × 3) and (4 × 4 × 4) yielded qualitatively very similar results compared to those using a 120-atom supercell, with respect to both structural distortions and the resulting electronic structure, rendering the 120-atom supercell a reasonable compromise with respect to computational cost. Charged cells were not considered as this is only relevant in the dilute limit, where the concentration of oxygen vacancies is too small to give rise to experimentally detectable chemical expansion. The Brillouin zone was sampled using a Γ-centered 3 × 3 × 2 mesh. Structures and cells were relaxed until forces on ions converged below 10^{-3} eV $Å^{-1}$. The materials under investigation and their ground state space groups considered here are listed in Table 1. Spin-polarized calculations were performed for both manganites and titanates. A G-type magnetic order was imposed on all manganite compounds in accordance with experimental reportings for $CaMnO_3$[49] and $SrMnO_3$.[50] A ferromagnetic order was imposed on the titanate compounds, supported by experimentally detected magnetism upon oxygen vacancy formation in $SrTiO_3$.[51]

Table 1. Summary of Considered Material Systems and the Considered Ground State Space Group, Glazer Tilt Pattern, Number of Inequivalent Oxygen Sites, and Tolerance Factor, *t*

material	space group	no. of inequivalent V_O	t[64]
$CaMnO_3$	*Pbnm* ($a^-a^-c^+$)[33]	2	0.977
$SrMnO_3$	$R\bar{3}c$ ($a^-a^-a^-$)[11]	1	1.033
$BaMnO_3$	*Amm*2 ($a^0a^0a^0$)[31]	2	1.097
$CaTiO_3$	*Pbnm* ($a^-a^-c^+$)[65]	2	0.946
$SrTiO_3$	*I*4/*mcm* ($a^0a^0c^-$)[37]	2	1.001
$BaTiO_3$	*R*3*m* ($a^0a^0a^0$)[38]	1	1.063

https://dx.doi.org/10.1021/acs.jpcc.0c02060
J. Phys. Chem. C 2020, 124, 12922−12932

On-site electron−electron repulsion, sometimes referred to as correlation, can be explicitly treated in DFT by tuning the Hubbard U parameter (DFT+U).[52,53] A range of different Hubbard U values have been in used in the literature[54] to describe one single material depending on the specific property to be optimized. Bandgap, lattice parameters, and phonon frequencies are examples of properties that are highly sensitive to the choice of Hubbard U. Hybrid functional approaches using Kohn−Sham orbitals with a weighted exchange defined in the Hartree−Fock theory are generally considered a more accurate approach for on-site electron repulsion or correlation[55] but hybrid functionals are much more computationally expensive than the DFT+U method. Hybrid functionals have been used as a benchmark to find suitable U values for the Mn 3d states, as was done for $CaMnO_3$, $SrMnO_3$, and $BaMnO_3$[56] resulting in U = 3.0, 2.8, 2.7 eV, respectively. This was achieved by comparing energy differences between antiferromagnetic and ferromagnetic exchange with HSE functionals and fitting energy differences obtained with U. However, the DFT+U method may better reproduce experimental results on oxygen vacancies in transition metal oxides, as reported by Santana et al.[57,58] Ti 3d states have also been treated with a range of Hubbard U values in the literature, typically around ∼2−5 eV[59−61] in perovskites. There have been even larger variations in U reported when Ti 3d states are modeled in binary titanate oxides ranging from 2 to 10 eV.[62] In this work, we exploit that Hubbard U can be tuned in the interval 0−5 eV to elucidate the effect of electron localization on structural distortions around an oxygen vacancy and the resulting chemical expansion effects. An effective Hubbard U was applied using Dudarev's method[63] in this work. Lattice parameters were optimized separately for each Hubbard U value used, so that volume changes upon vacancy formation refer self-consistently to the U-specific relaxed lattice parameters.

RESULTS

Structural Distortions and Chemical Expansion. We first consider structural distortions caused by the formation of an oxygen vacancy in a charge neutral supercell corresponding to an oxygen deficiency of δ = 0.0414 and with fixed lattice parameters to simulate a low concentration (dilute limit). We show the structural distortions in $CaMnO_{3-\delta}$ and $CaTiO_{3-\delta}$ as a function of distance from the oxygen vacancy in Figure 1. For simplicity, we refer to stoichiometric compounds in the following although they are oxygen deficient. The displacements are shown for U = 0 eV (blue symbols) and U = 5 eV (yellow symbols). Since equilibrium volumes are sensitive to the choice of Hubbard U, the ionic displacements are scaled with the cube root of the equilibrium volume for each value of U. The qualitative distortions around an oxygen vacancy are similar for both the manganites and the titanates. The largest ionic distortions occur in the nearest and next nearest coordination shell of the oxygen vacancy, where the electrostatic forces are strongest. Since the oxygen vacancy has a relative charge of +2, positively charged nearest neighbor ions are displaced away from the vacancy whereas the negatively charged oxygen ions displace toward the vacancy as expected from electrostatic considerations. The charge compensation of the oxygen vacancy, usually described as formation of electrons or reduced Ti/Mn, is a key point in the following. The effect of choice of Hubbard U is very different when $CaMnO_3$ and $CaTiO_3$ are compared. Whereas U = 0 eV and U = 5 eV only show subtle effects on the degree of structural distortions

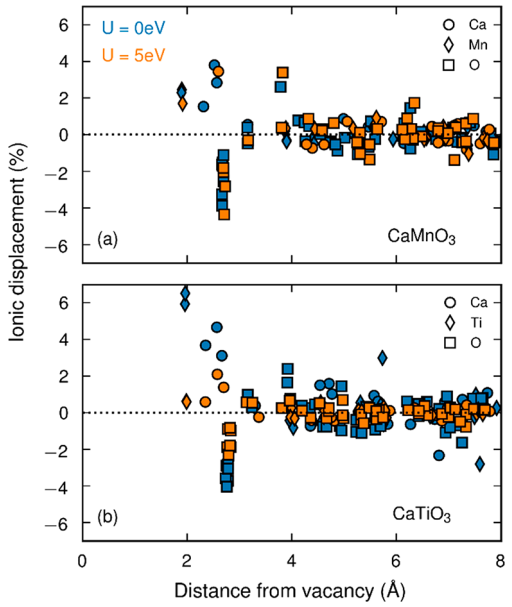

Figure 1. Ionic displacements as a function of distance from an oxygen vacancy in (a) $CaMnO_{3-x}$ and (b) $CaTiO_{3-x}$ calculated with fixed lattice vectors. Positive (negative) ionic displacements represent a displacement away from (closer to) the vacancy site. The ionic displacements are given relative the cube root of the unit cell volume. Comparison of distortions with Hubbard U = 0 eV (blue) and Hubbard U = 5 eV (yellow) is also shown.

around the oxygen vacancy in $CaMnO_3$, there is a significant reduction in the ionic displacements around the O vacancy when Hubbard U is increased in $CaTiO_3$.

To compare the degree of structural distortions around an oxygen vacancy for all compounds as a function of Hubbard U, we consider the nearest neighbor (NN) ionic displacements in the A and B sublattice around the vacancy. There are four nearest neighbor A cations and two nearest neighbor B cations to the oxygen vacancy. The average distortion length $\langle\delta_{NN}\rangle$ of the NN_A cations and NN_B cations can be defined by

$$\langle\delta_{NN}\rangle = \frac{1}{6}\left(\sum \delta_{NN_A} + \sum \delta_{NN_B}\right) \quad (2)$$

The average NN distortion length with fixed lattice vectors as a function of Hubbard U is plotted in Figure 2a (manganites) and Figure 2b (titanates). These distortions are scaled with the cube root of the equilibrium volume for each Hubbard U to give comparable values. Some of the materials have symmetry inequivalent oxygen sites; however, distortion lengths are here only given upon breaking a B−O bond along the c-axis. Distortion lengths upon breaking a B−O bond within the ab-plane are omitted for clarity, as these results are quantitatively very similar. Space group settings are listed in Table 1.

The general trend seen for the manganite compounds is a subtle increase in distortions with increasing Hubbard U. Moreover, the average distortion length for the NN cations are very similar in all the manganites. In contrast, the titanates display different distortion regimes within the range of U values considered here. Whereas there are large distortions of the nearest neighbor cations upon V_O formation for low U values, there is a significant and sharp decrease in structural distortions with increased Hubbard U (Figure 2b). Furthermore, even though the titanates follow the same trend, the

https://dx.doi.org/10.1021/acs.jpcc.0c02060
J. Phys. Chem. C 2020, 124, 12922−12932

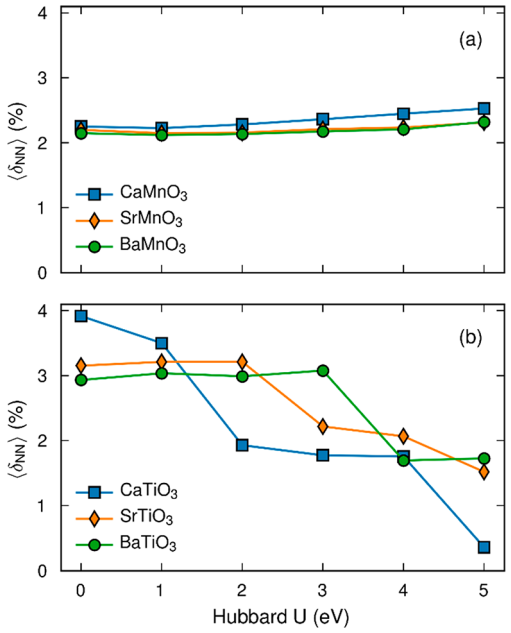

Figure 2. Average of NN_A (nearest neighbor A cations) and NN_B (nearest neighbor B cations) distortions in the (a) manganites and (b) titanates, calculated with fixed lattice vectors.

large decrease in average distortion length is shifted toward higher Hubbard *U* values with increased tolerance factor, i.e., from $CaTiO_3$ to $BaTiO_3$.

When the lattice vectors are allowed to relax, the resulting volume changes. The chemical expansion in response to the formation of an oxygen vacancy is shown in Figure 3a for the manganites and Figure 3b for the titanates. The trends in the resulting volume change correspond well with the nearest neighbor distortions, with a scale factor of approximately 0.1 (Figure 2a,b). Importantly, the short- and long-range structural response to oxygen vacancies is correlated. Local structural distortions around a vacancy hence have predictive power structural relaxations with fixed lattice vectors with respect to chemical expansion. Exceptions are found for the Ba-containing compounds, as is discussed further below. The corresponding total magnetic moment of the supercells are also shown in Figure 3. Whereas for the manganites, the total magnetic moment is constant equal to zero due to the antiferromagnetic ordering that is not altered by oxygen vacancy formation, the total magnetic moment in the titanates is, however, sensitive to Hubbard *U*.

Within the manganite series, $CaMnO_3$ and $SrMnO_3$ display very similar chemical expansion behaviors that are only weakly dependent on the Hubbard *U*. There is a stronger Hubbard *U* dependence of the volume change in $BaMnO_3$, even though the NN cation displacements with fixed lattice vectors are similar to those of $CaMnO_3$ and $SrMnO_3$. This can in part be attributed to the high sensitivity to changes in electronic structure, as polar distortions in $BaMnO_3$ are stabilized through empty Mn e_g orbitals,[31] giving rise to a directional second-order Jahn−Teller effect very similar to that found in ferroelectric titanates with d^0 Ti^{4+}. Oxygen vacancies thus compete with the polar distortions as charge compensating electrons occupy e_g orbitals on Mn ions adjacent to the vacancy.[11] Additionally, due to the large tolerance factor of $BaMnO_3$, the perovskite structure is thermodynamically much less stable than the preferred 2H hexagonal polymorph. This

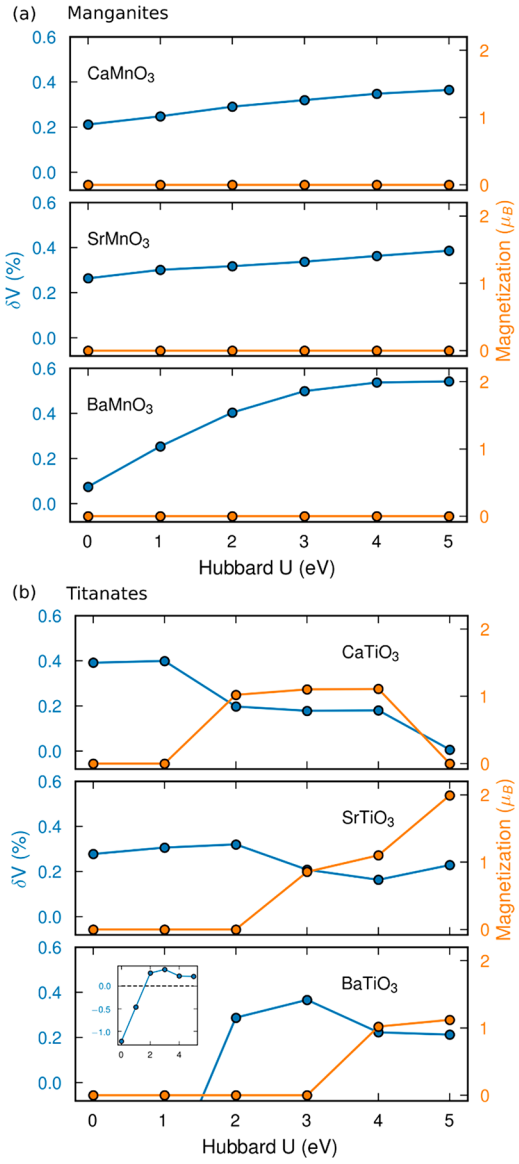

Figure 3. Calculated chemical expansion and total magnetization upon oxygen vacancy formation in (a) manganites and (b) titanates as a function of Hubbard *U*.

again results in large structural rearrangements to optimize the coordination environment of both Ba and Mn when the volume is allowed to change upon vacancy formation.

Within the titanates, $CaTiO_3$ and $SrTiO_3$ show strong correlation between NN structural distortions and chemical expansion. The larger NN distortions in $CaTiO_3$ with small Hubbard *U* values compared to those of $SrTiO_3$ also result in a larger chemical expansion in the "small *U*"-regime. Furthermore, the abrupt decrease in NN distortions with sufficiently large Hubbard *U* is also reflected in the volume change, with the same scaling. In $CaTiO_3$, the calculated chemical expansion starts to decrease at $U = 2$ eV, with a corresponding increase in magnetization from 0 μ_B to ∼1 μ_B. A total magnetization of ∼1 μ_B signifies partial electron localization, where one charge-compensating electron has localized whereas the second electron is still delocalized. At $U = 5$ eV, the magnetization again drops to 0 μ_B as the chemical expansion also is reduced to approximately zero. This is caused by electron-pairing of the two charge-compensation electrons, which are both localized

https://dx.doi.org/10.1021/acs.jpcc.0c02060
J. Phys. Chem. C 2020, 124, 12922−12932

at this U value. In $SrTiO_3$, the chemical expansion starts to decrease at U = 3 eV, with the corresponding magnetization increasing from 0 μ_B to ∼1 μ_B. At U = 5 eV, there is, in contrast to $CaTiO_3$, a slight increase again in the chemical expansion with the corresponding total magnetization increasing to ∼2 μ_B, signifying localization of both charge-compensating electrons with ferromagnetic alignment.

$BaTiO_3$ does not display a simple correlation between NN distortions and the corresponding chemical expansion, as the calculated chemical expansion is negative for small values of U and only becomes positive for a sufficiently large value of U (≥2 eV). The explanation for this is 2-fold: First, when an oxygen vacancy is formed and the on-site repulsion is weak (small Hubbard U), the charge compensating electrons are itinerant, causing $BaTiO_{3-x}$ to become metallic, which again screens the ferroelectric polarization. When the cell volume is allowed to change, it then contracts due to a polar to nonpolar phase transition. Second, when Hubbard U is sufficiently increased, this also suppresses the polar offset of the Ti ions in the absence of an oxygen vacancy. The underlying mechanism for polarization in $BaTiO_3$ is the second-order Jahn−Teller effect (as also for $BaMnO_3$), relying on a stabilizing partial covalent bonds between O 2p orbitals and empty Ti 3d orbitals. When Hubbard U is increased, the energy cost to charge transfer electrons from O to Ti increases to the extent that polarization is completely suppressed for Hubbard $U \geq 2$ eV. Thus, the shift to a positive chemical expansion with increased Hubbard U is a combined effect of increased localization of charge compensating electrons upon vacancy formation and a Hubbard U driven phase transition from polar to nonpolar symmetry. The total magnetization is 0 μ_B at all U values below U = 4 eV, where, as for $CaTiO_3$ and $SrTiO_3$, a reduction of the chemical expansion at this value is accompanied by an increase in the total magnetization to ∼1 μ_B, again signifying partial localization of the charge-compensating electrons.

Chemical expansion is not isotropic on a microscopic length scale. The anisotropic relaxation of a, b and c lattice parameters upon formation of an oxygen vacancy is shown in Figure 4 for the manganites and Figure 5 for the titanates. The anisotropic strain where B−O bonds parallel to the $a(c)$-axis are broken is shown in the left (right) columns. The largest chemical strain is generally found along the broken B−O bond in both the manganites and the titanates. The resulting relaxation along the perpendicular axes is dependent on both the space group and the B cation and thus varies significantly between the considered materials. In $CaMnO_3$, the perpendicular axes are barely affected by formation of an oxygen vacancy. This is in contrast with the Sr-containing compounds where all three lattice parameters are highly sensitive to V_O formation. This can be understood in terms of their intermediate tolerance factor, resulting in larger sensitivity of their ground state structures to small volume changes. In tetragonal $SrTiO_3$, both the symmetry inequivalent oxygen vacancies cause contraction of the elongated c axis, and expansion along the two other axes, making the structure more cubic. This is in line with an increased effective tolerance factor upon V_O formation. $BaMnO_3$ displays significantly larger strain along the broken B−O bond than the other material systems, which again is reasoned by both a high sensitivity to changes in electronic structure and a large driving force for structural rearrangements due to the high thermodynamic cost of attaining the perovskite structure, as discussed above.

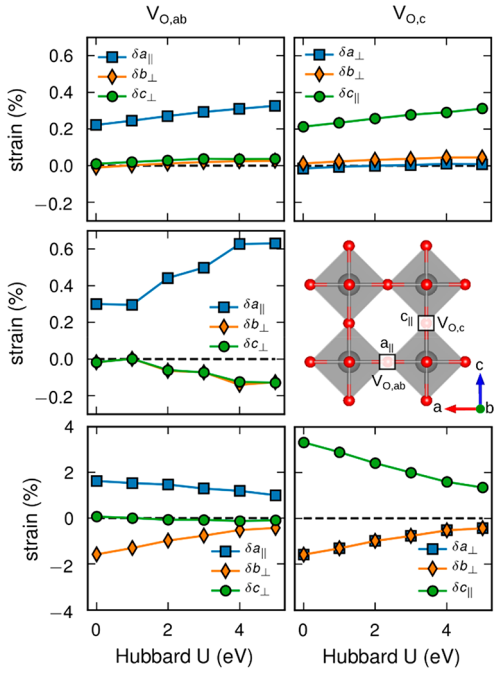

Figure 4. Anisotropic chemical expansion as a function of Hubbard U within the manganites, shown for vacancy formation with a broken Mn−O bond parallel to the a-axis (left column) and c-axis (right column). Only one panel is shown for $SrMnO_3$ due to crystal symmetry.

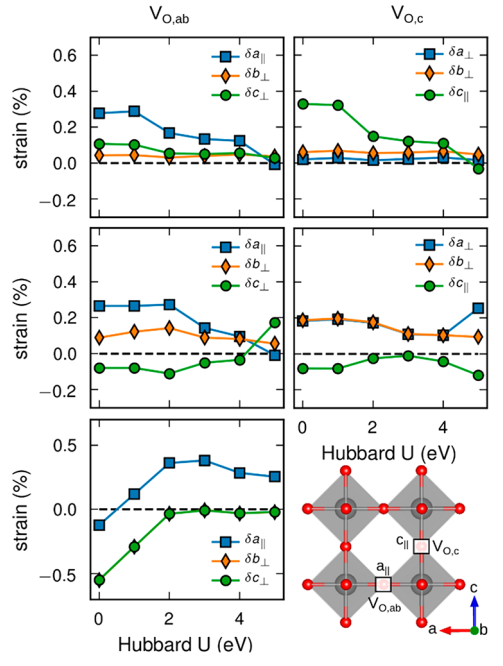

Figure 5. Anisotropic chemical expansion as a function of Hubbard U within the titanates, shown for vacancy formation with a broken Mn−O bond parallel to the a-axis (left column) and c-axis (right column). Only one panel is shown for $BaTiO_3$ due to crystal symmetry.

Electron Localization. The degree of electron localization as a function of Hubbard U was quantified by calculating the Bader charges[66] and further defined by

$$dQ_{B\ site} = Q_{B\ site,NN} - Q_{B\ site,bulk} \quad (3)$$

https://dx.doi.org/10.1021/acs.jpcc.0c02060
J. Phys. Chem. C 2020, 124, 12922−12932

where $Q_{B\ site,\ NN}$ is the average of the Bader charge of the two nearest neighbor B cations to the oxygen vacancy, $Q_{B\ site,\ bulk}$ is the average Bader charge of the bulk B cations, and $dQ_{B\ site}$ defines the difference between these two quantities. The degree of electron localization defined by eq 3 as a function of Hubbard U is shown in Figure 6a (manganites) and Figure 6b (titanates). The average bulk Bader charges are shown in the insets of Figure 6a,b. The degree of localization is highly insensitive to the Hubbard U parameter in the manganites. In contrast, charge localization in the titanates is much more sensitive to Hubbard U, with a difference in $dQ_{B\ site,\ NN}$ of ~0.35e for $CaTiO_3$, ~0.25e for $SrTiO_3$, and ~0.15e for $BaTiO_3$ across the range of U = 0 eV to U = 5 eV. The localization does not show a linear trend with U, and the three titanates show different robustness with respect to U, respectively: the smaller the tolerance factor the less on-site electron repulsion (smaller Hubbard U) is needed for the charge compensating electrons to localize. Furthermore, we see a direct correlation between the degree of structural distortions with corresponding chemical expansion (Figure 3) and the degree of electron localization (Figure 6). The structural response to oxygen vacancies is thus strongly coupled to the valency reduction of the transition metal cations.

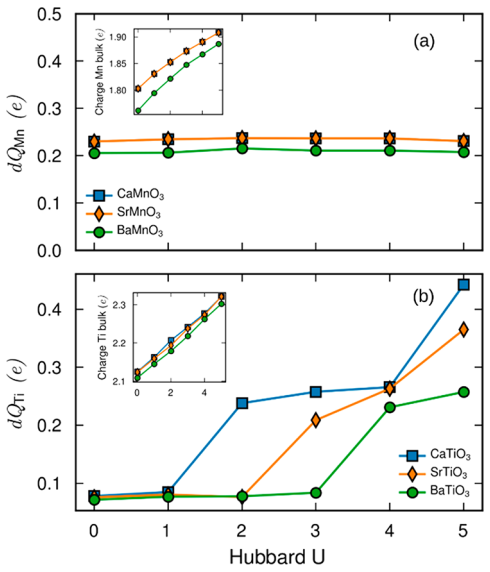

Figure 6. Degree of electron localization as a function of Hubbard U. Charge localization dQ as defined in eq 3 shown for (a) the manganite and (b) the titanate series. The insets show the average bulk Bader charge as a function of Hubbard U.

To understand the different localization trends with Hubbard U, one cannot consider the Hubbard U term alone, since the degree of electronic localization in a compound also depends on the electronic bandwidth. The relevant parameter governing electronic localization is the ratio U/W, where W is the electronic bandwidth. In perovskites, W is proportional the orbital overlap in space and energy between O 2p and transition metal 3d orbitals,[67] which again governs the magnitude of the 3d−3d charge transfer integral. The spatial overlap between these orbitals again depends on the B−O−B bond angle ϕ. A lower tolerance factor implies a more distorted perovskite structure with smaller B−O−B bond angles and concomitantly less overlap between B 3d and O 2p

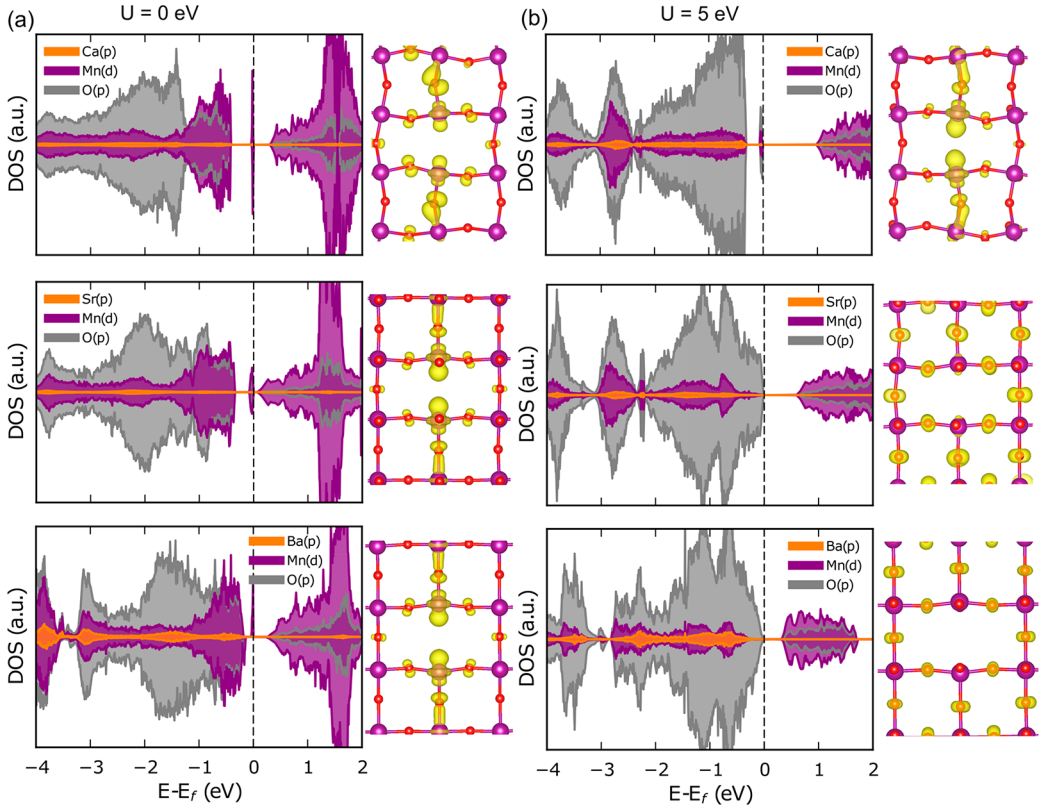

Figure 7. Calculated partial charge density in the energy interval from the Fermi level to 0.3 eV below and density of states of defect state in the manganite oxides, shown for Hubbard U = 0 eV (a) and Hubbard U = 5 eV (b).

https://dx.doi.org/10.1021/acs.jpcc.0c02060
J. Phys. Chem. C 2020, 124, 12922−12932

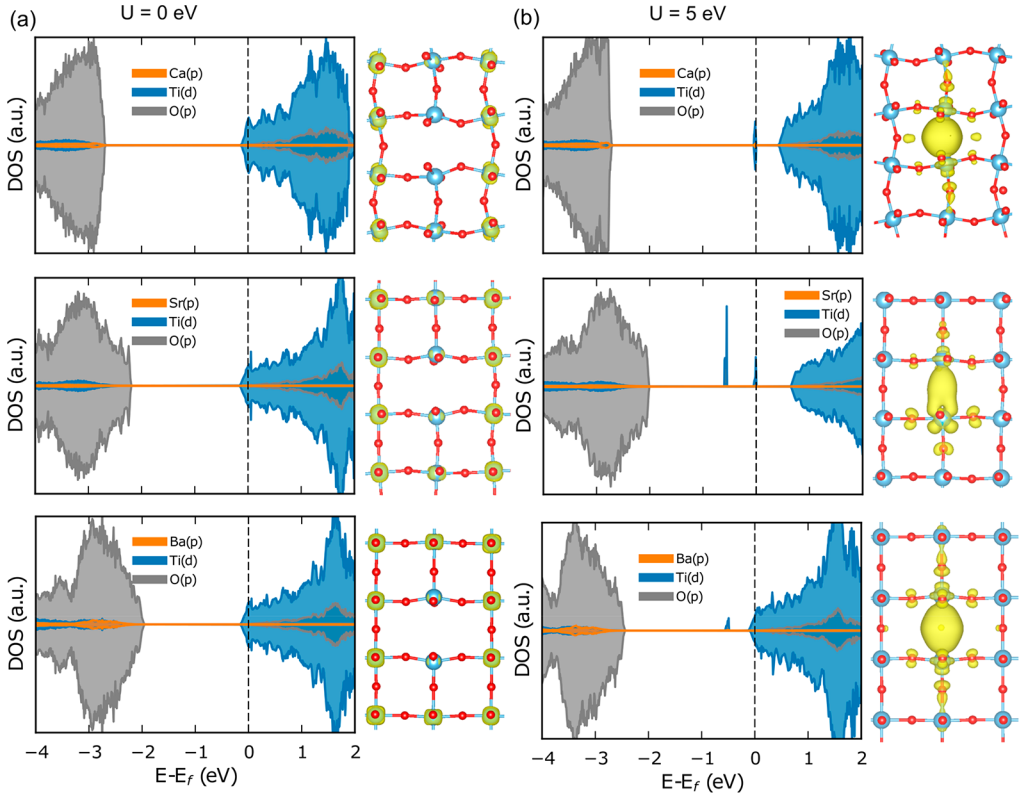

Figure 8. Calculated partial charge density in the energy interval from the Fermi level to 1 eV below and density of states of defect state in the titanate oxides, shown for Hubbard U = 0 eV (a) and Hubbard U = 5 eV (b).

orbitals. The smaller orbital overlap in turn results in a smaller 3d−3d charge transfer integral, favoring electron localization.

When the tolerance factor is increased, from $CaTiO_3$ to $SrTiO_3$ to $BaTiO_3$, the Ti−O−Ti bond angles ϕ approach 180°, and the orbital overlap and electronic bandwidth W increases. As a consequence, when $BaTiO_3$ becomes cubic with $U \geq 2$ eV, the ratio U/W decreases, and a larger U is necessary for the charge compensating electrons to localize. This is also reflected by the larger Hubbard U values needed to achieve localization when the tolerance factor increases. In the manganites, however, the orbital overlap between O 2p and 3d is already spatially much smaller than in the titanates (although the orbitals are much closer in energy) yielding localized electrons also for small values of Hubbard U. Therefore, electron localization in the manganites is insensitive to Hubbard U (Figure 6).

Electronic Structure. We now look at the underlying electronic mechanisms driving the different localization behaviors in manganites and titanates by exploring the effect on Hubbard U on the density of states. The electronic density of states and the charge density of the defect state for different Hubbard U values for the manganites and titanates are displayed in Figures 7 and 8, respectively. The electronic bandgap in the manganites is defined by the energy difference between the triply occupied t_{2g} states and the e_g states, in other words by the octahedral crystal field splitting. In the titanates, however, the bandgap is between O 2p states dominating the valence band maximum and empty Ti 3d states defining the conduction band minimum and is thus equal to the charge transfer energy, ΔE. The bandgaps in the titanate series are much larger than in the manganites, as seen in Figures 7 and 8.

We first discuss the manganites (Figure 7). The defect state is already localized for small values of Hubbard U. For U = 0 eV, the partial charge density clearly illustrates the e_g orbitals occupied with the two charge compensating electrons on two Mn cations adjacent to the vacancy. Increasing the Hubbard U on the Mn d states shifts occupied states down in energy and unoccupied Mn d states up in energy. Thus, the defect state is shifted closer to the valence band edge. The calculated Bader charges on Mn, shown in the inset of Figure 6a, of about +1.8−1.9, are well below the formal oxidation state +4, and indicate strong covalency between Mn 3d orbitals and O 2p states. The bonding orbitals are stabilized by $\Delta\epsilon = b^2/\Delta E$, i.e., proportional to the square of the hopping integral b, and inversely proportional to the charge transfer energy ΔE.[67] The Mn d states lie close to O 2p in energy, and this is reflected by the partial transfer of the charge compensating electron density to neighboring oxygen ions. With increasing Hubbard U, the defect state is shifted toward the valence band edge, the charge transfer to oxygen increases, as illustrated with the partial charge density plots in Figure 6, and an increased O partial charge density in the defect state in the DOS.

Second, we discuss the electronic structure in the titanates by comparing U = 0 and U = 5 eV results for all three compounds (Figure 8). The defect state for U = 0 eV is located in the conduction band, resulting in itinerant charge compensating electrons that are distributed over all the Ti in the supercell. This can be seen in the partial charge density plots that clearly show the shape of the t_{2g} orbitals. This is also consistent with the net zero magnetization in the titanates at low Hubbard U values. Upon further localization of the charge compensating electrons, isolated defect states are formed close to the conduction band, as observed for U = 5 eV in Figure 8.

https://dx.doi.org/10.1021/acs.jpcc.0c02060
J. Phys. Chem. C 2020, 124, 12922−12932

However, as indicated by the varying magnetization with Hubbard U for the titanates, there are different degrees of localization with increasing U. In the regime where the magnetization is ~1 μ_B, then one charge-compensating electron localizes at the defect site, whereas the other electron is still delocalized in the supercell. This is also the most stable electron configuration for $BaTiO_3$ at 5 eV, as seen in Figure 8. $SrTiO_3$ has been reported to both produce a deep level state in the band gap and be an electron donor upon oxygen vacancy formation.[68] This is consistent with such an electronic structure stabilized for $SrTiO_3$ between U = 3 and 4 eV. Contrary to the manganites, the electrons tend to localize on the vacancy site forming a so-called F-center, as is also previously reported for $SrTiO_3$,[61,69] and reflects an unstable Ti^{3+} oxidation state. The two Ti dangling bonds combine into bonding and antibonding states composed mostly of d_{z^2}, which the charge-compensating electron occupies. The formation of an F-center provides strong electrostatic screening of the vacancy and reduces the local structural distortions significantly. In $CaTiO_3$ and $SrTiO_3$, U = 5 eV localizes both charge-compensating electrons; however, the resulting electronic structures differ. In $CaTiO_3$, the second electron also localizes on the vacancy site with d_{z^2} character, resulting in almost net zero chemical expansion and magnetization equal to 0 μ_B. In contrast, in $SrTiO_3$, the second electron localizes on a Ti t_{2g} orbital, which is ferromagnetically coupled with the initially localized electron, giving rise to a net magnetization of ~2 μ_B.

Energetics. The calculated formation energies of an oxygen vacancy in a charge neutral cell, defined by

$$E_{form} = E_{tot,V_O} - E_{tot,Stoich} + \mu_O \quad (4)$$

are shown in Figure 9, which correlate well with the evolution of the electronic structures, as seen in Figure 7 (manganites) and Figure 8 (titanates). Symmetry inequivalent oxygen vacancies have very similar formation energies with variations within 0.01 eV; hence, the average formation energies are shown. As the vacancy concentration is higher than in the dilute limit, the calculated energies are strictly speaking enthalpies of reduction. The formation energies of the manganites are lower than those of the titanates, consistent with previous reports.[70] Trends in the tolerance factor are also clearly reflected: the oxygen vacancy formation energies correlate with the electronic bandgap, which for the manganites is defined by the crystal field splitting. The crystal field splitting decreases with increasing tolerance factor as the size of the BO_6 octahedra increases. With increasing Hubbard U, the vacancy formation energies are reduced in accordance with the defect state approaching the valence band edge. Similarly, for the titanates, the bandgap is defined by the energy difference between O 2p and t_{2g} states. In contrast to the manganites, the vacancy formation energies increase with increasing Hubbard U to the point where the localized defect state is lower than the conduction band edge, where the formation energy flattens out.

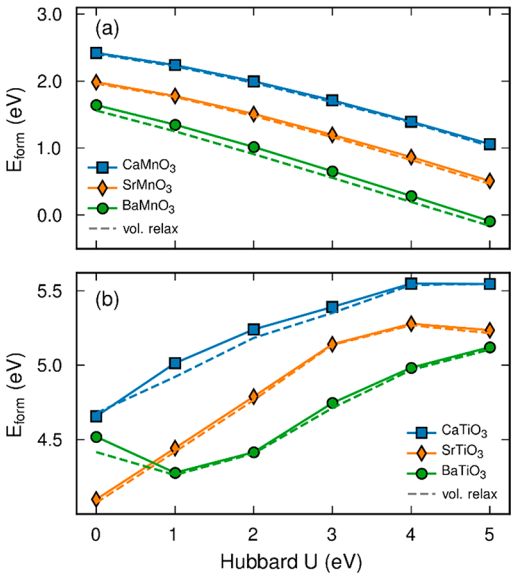

Figure 9. Calculated oxygen vacancy formation energies as a function of Hubbard U for (a) manganites and (b) titanates, with a chosen oxygen chemical potential of −5 eV. Solid lines show the vacancy formation energy with fixed lattice vectors whereas dashed lines show the formation energy with relaxed lattice vectors.

DISCUSSION

Here we have studied chemical expansion upon oxygen vacancy formation in manganite and titanate perovskites, and the underlying mechanisms driving the volume change, with emphasis on the effect of on-site electron repulsion (Hubbard U). In the manganites, increasing the Hubbard U parameter yields only subtle changes in structural distortions and resulting chemical expansion. The insensitivity of the manganites to the U value is due to the narrow 3d bandwidth, which yields localized charge compensating electrons even in the absence of an imposed Hubbard U. This again stems from the smaller spatial extension of the 3d orbitals as seen from the Shannon radius of Mn^{4+} (0.53 Å) compared to that of Ti^{4+} (0.605 Å). In the titanates, varying the Hubbard U parameter has a large effect on the chemical expansion, as the electronic configuration changes from having delocalized charge-compensating electrons to highly localized electrons, which again strongly affects the structural distortions around the vacancy.

There are clear tolerance factor trends among the titanates with respect to the robustness of the itinerant electron regime with variation in Hubbard U. However, the degree of chemical expansion does not show any clear correlation with the tolerance factor dependence for either the titanates or the manganites. Ferroelectricity in the Ba-containing compounds with high tolerance factors complicates the search for trends as oxygen vacancies impede ferroelectric distortions,[11] which is a different mechanism causing (anisotropic) lattice expansion. This effect will, however, be less pronounced at elevated temperatures where the polarization induced strain is reduced or lost. Moreover, there are also only subtle differences in the chemical expansion calculated for the manganites, having localized charge-compensating electrons and for the titanates in the itinerant electron regime. Hence, the structural distortion lengths due to the vacancy are very similar even though the electronic structures are quite different in the manganites and titanates.

The degree of chemical expansion calculated in this work is limited to a specific concentration of oxygen vacancies (δ = 0.0414). Chemical expansion is, however, highly dependent on the concentration and distribution of vacancies, and the chemical expansion coefficient must be expected to depend on the vacancy concentration as shown by Chen et al.[21] A point defect concentration-dependent nonlinear chemical expansion

https://dx.doi.org/10.1021/acs.jpcc.0c02060
J. Phys. Chem. C 2020, 124, 12922−12932

coefficient was, e.g., also found computationally for oxygen interstitials in bixbyite V_2O_3 nanocrystals.[71]

Following the formal definition of chemical expansion in eq 1, there is no lower concentration threshold for chemical expansion. However, in the dilute limit, where oxygen vacancies are fully isolated ($\delta \sim 0$) in the sense that there is no overlap between the elastic strain fields between individual vacancies, the effect of each individual point defect is completely screened. That is, the *effective* screening length is shorter than the average distance between adjacent vacancies, and the resulting chemical expansion would be local and could easily elude experimental detection. When the distortion volumes of individual vacancies start to overlap, i.e., when the average V_O−V_O distance becomes smaller than the effective vacancy screening length, the material will experience chemical expansion that can be experimentally detected from the lattice parameters or macroscopic sample dimensions. This occurs when the oxygen vacancy concentration reaches a certain percolation threshold, assuming that general percolation theory applies. The percolation threshold is further dependent on the effective distortion volume around a vacancy, in analogy to strain fields in deformed metals.[72] A *percolation* threshold defines the critical vacancy concentration, $[V_O]_c$, at which there exists a spanning cluster of interacting strain fields. Below this concentration, there will be no *experimentally detectable* chemical expansion, and above this concentration, an increasing chemical expansion δV will be observed and can be described by

$$\begin{aligned} \delta V &= 0 \quad \text{if } [V_O] < [V_O]_c \\ &\geq 0 \quad \text{if } [V_O] \geq [V_O]_c \end{aligned} \tag{5}$$

In the itinerant electron regime for the titanates, the percolation threshold will be similar to that of the manganites. However, if F-centers are formed in the titanates, the percolation threshold is much larger than in manganites with comparably larger distortion volumes.

General predictions on how charge compensating electrons upon V_O formation localize in transition metal oxides are not straightforward to make. In this respect, transition metal oxides differ from rare earth oxides where f-electrons are always localized, or from s- and p-block metal oxides where charge compensating electrons in the conduction band will generally be delocalized due to the large overlap of s- and p-orbitals. The comparatively intermediate electron localization in the d-block oxides gives rise to both a multitude of functional properties and the demonstrated complexity with respect to chemical expansion. In contrast, for f-block CeO_2 chemical expansion increases monotonically with Hubbard U as the f-electrons are strongly localized.[1,2]

A study comparing V_O formation in $LaFe^{3+}O_3$ with that in $SrFe^{4+}O_3$ highlighted the importance of electron configuration on polaron size in ferrites. V_O formation in $LaFeO_3$ gives localized charge compensating electrons on neighboring Fe cations, whereas they localize on *next* nearest neighboring Fe cations in $SrFeO_3$ due to differences in available energy levels in the distorted crystal field.[73] Here, the different localization behaviors of the II−IV manganites and titanates are attributed to differences in B−O bond covalency as well as the stability of the resulting redox state of the B cation. The $A^{3+}CrO_3$ family, with iso-electronic d^3 configuration of the Mn^{4+} and Cr^{3+} cations could thus be expected to show electronic localization behavior very similar to that of the II−IV manganites. The weaker Cr−O covalency would, however, be expected to yield better screening of the oxygen vacancy as less charge is transferred onto the Cr−O bonds.

The concentration of oxygen vacancies in transition metal oxides can be tuned by temperature and atmosphere. The higher the temperature and lower the oxygen partial pressure, the larger the equilibrium concentration of oxygen vacancies. On the basis of the calculated oxygen vacancy formation energies of the manganites and the titanates, one would, however, require a lower partial pressure of oxygen in the titanates to acquire the same vacancy concentration levels as in the manganites. Furthermore, the degree of electron localization, and hence also the degree of chemical expansion, can be tuned by, e.g., epitaxial strain or isovalent doping on the A site. These approaches could structurally and chemically expand or contract the bulk structure, which again tunes the electronic bandwidth.

CONCLUSIONS

In this work, we have carried out first-principles calculations to study the chemical expansion of alkaline earth Mn and Ti perovskite oxides due to formation of oxygen vacancies accompanied by reduction of Mn/Ti. The chemical expansion was explicitly calculated for the two series Ca, Sr, and Ba manganites and titanates. The focus in the evaluation of the phenomena is the evolution of structural and electronic behavior with on-site electron repulsion by systematically varying the Hubbard U. Increasing the Hubbard U on the B site resulted in increased chemical expansion in the manganites and reduced chemical expansion in the titanates, arising from large differences in electrostatic screening of the oxygen vacancy. The effect was attributed to differences in electronic energy levels and the relative difference in covalency of the Mn−O and Ti−O bonds. The effect of on-site electron repulsion is much more complex in transition metal oxides than in, e.g., rare earth oxides, as d-electrons are more prone to delocalization than strongly localized f-electrons. A detailed understanding of the electronic structure and chemical bonds is necessary for rational design of chemical expansion for materials for solid state ionics, sensor and actuator applications.

ASSOCIATED CONTENT

Supporting Information

The Supporting Information is available free of charge at https://pubs.acs.org/doi/10.1021/acs.jpcc.0c02060.

Table summarizing stoichiometric pseudocubic lattice parameters and resulting lattice parameters after volume relaxation upon oxygen vacancy formation for U = 0 eV and U = 5 eV (PDF)

AUTHOR INFORMATION

Corresponding Author

Sverre M. Selbach − *Department of Materials Science and Engineering, NTNU Norwegian University of Science and Technology, 7491 Trondheim, Norway;* orcid.org/0000-0001-5838-8632; Email: selbach@ntnu.no

Authors

Astrid Marthinsen − *Department of Materials Science and Engineering, NTNU Norwegian University of Science and Technology, 7491 Trondheim, Norway*

https://dx.doi.org/10.1021/acs.jpcc.0c02060
J. Phys. Chem. C 2020, 124, 12922−12932

Tor Grande − *Department of Materials Science and Engineering, NTNU Norwegian University of Science and Technology, 7491 Trondheim, Norway*

Complete contact information is available at: https://pubs.acs.org/10.1021/acs.jpcc.0c02060

Notes

The authors declare no competing financial interest.

■ ACKNOWLEDGMENTS

The work was supported by NTNU and the Research Council of Norway, FRINATEK project 231430. Computational resources were provided by UNINETT Sigma2 through the project NN9264K.

■ REFERENCES

(1) Adler, S. B. Chemical Expansivity of Electrochemical Ceramics. *J. Am. Ceram. Soc.* **2001**, *84*, 2117−2119.
(2) Marrocchelli, D.; Bishop, S. R.; Tuller, H. L.; Watson, G. W.; Yildiz, B. Charge Localization Increases Chemical Expansion in Cerium-Based Oxides. *Phys. Chem. Chem. Phys.* **2012**, *14*, 12070−12074.
(3) Marrocchelli, D.; Bishop, S. R.; Tuller, H. L.; Yildiz, B. Understanding Chemical Expansion in Non-Stoichiometric Oxides: Ceria and Zirconia Case Studies. *Adv. Funct. Mater.* **2012**, *22*, 1958−1965.
(4) Marrocchelli, D.; Perry, N. H.; Bishop, S. R. Understanding Chemical Expansion in Perovskite-Structured Oxides. *Phys. Chem. Chem. Phys.* **2015**, *17*, 10028−10039.
(5) Tao, S. W.; Irvine, J. T. S.; Kilner, J. A. An Efficient Solid Oxide Fuel Cell Based upon Single-Phase Perovskites. *Adv. Mater.* **2005**, *17*, 1734−1737.
(6) Bishop, S. R.; Marrocchelli, D.; Chatzichristodoulou, C.; Perry, N. H.; Mogensen, M. B.; Tuller, H. L.; Wachsman, E. D. Chemical Expansion: Implications for Electrochemical Energy Storage and Conversion Devices. *Annu. Rev. Mater. Res.* **2014**, *44*, 205−239.
(7) Atkinson, A.; Ramos, T. M. G. M. Chemically-Induced Stresses in Ceramic Oxygen Ion-Conducting Membranes. *Solid State Ionics* **2000**, *129*, 259−269.
(8) Sato, K.; Omura, H.; Hashida, T.; Yashiro, K.; Yugami, H.; Kawada, T.; Mizusaki, J. Tracking the Onset of Damage Mechanism in Ceria-Based Solid Oxide Fuel Cells under Simulated Operating Conditions. *J. Test. Eval.* **2006**, *34*, 246−250.
(9) Swallow, J. G.; Kim, J. J.; Maloney, J. M.; Chen, D.; Smith, J. F.; Bishop, S. R.; Tuller, H. L.; Van Vliet, K. J. Dynamic Chemical Expansion of Thin-Film Non-Stoichiometric Oxides at Extreme Temperatures. *Nat. Mater.* **2017**, *16*, 749−754.
(10) Aschauer, U.; Pfenninger, R.; Selbach, S. M.; Grande, T.; Spaldin, N. A. Strain-Controlled Oxygen Vacancy Formation and Ordering in $CaMnO_3$. *Phys. Rev. B: Condens. Matter Mater. Phys.* **2013**, *88*, 54111.
(11) Marthinsen, A.; Faber, C.; Aschauer, U.; Spaldin, N. A.; Selbach, S. M. Coupling and Competition between Ferroelectricity, Magnetism, Strain, and Oxygen Vacancies in $AMnO_3$ Perovskites. *MRS Commun.* **2016**, *6*, 182−191.
(12) Chandrasena, R. U.; Yang, W.; Lei, Q.; Delgado-Jaime, M. U.; Wijesekara, K. D.; Golalikhani, M.; Davidson, B. A.; Arenholz, E.; Kobayashi, K.; Kobata, M.; et al. Strain-Engineered Oxygen Vacancies in $CaMnO_3$ Thin Films. *Nano Lett.* **2017**, *17*, 794−799.
(13) Jedvik, E.; Lindman, A.; Benediktsson, M. P.; Wahnström, G. Size and Shape of Oxygen Vacancies and Protons in Acceptor-Doped Barium Zirconate. *Solid State Ionics* **2015**, *275*, 2−8.
(14) Perry, N. H.; Kim, J. J.; Bishop, S. R.; Tuller, H. L. Strongly Coupled Thermal and Chemical Expansion in the Perovskite Oxide System Sr(Ti,Fe)O 3-δ. *J. Mater. Chem. A* **2015**, *3*, 3602−3611.
(15) Fossdal, A.; Menon, M.; Waernhus, I.; Wiik, K.; Einarsrud, M.-A.; Grande, T. Crystal Structure and Thermal Expansion of La1−xSrxFeO3−δ Materials. *J. Am. Ceram. Soc.* **2004**, *87*, 1952−1958.
(16) Kuhn, M.; Hashimoto, S.; Sato, K.; Yashiro, K.; Mizusaki, J. Oxygen Nonstoichiometry, Thermo-Chemical Stability and Lattice Expansion of $La_{0.6}Sr_{0.4}FeO_{3-\delta}$. *Solid State Ionics* **2011**, *195*, 7−15.
(17) Kuhn, M.; Hashimoto, S.; Sato, K.; Yashiro, K.; Mizusaki, J. Oxygen Nonstoichiometry and Thermo-Chemical Stability of $La_{0.6}Sr_{0.4}CoO_{3-\delta}$. *J. Solid State Chem.* **2013**, *197*, 38−45.
(18) Kriegel, R.; Kircheisen, R.; Töpfer, J. Oxygen Stoichiometry and Expansion Behavior of $Ba_{0.5}Sr_{0.5}Co_{0.8}Fe_{0.2}O_{3-\delta}$. *Solid State Ionics* **2010**, *181*, 64−70.
(19) Hashimoto, S.; Fukuda, Y.; Kuhn, M.; Sato, K.; Yashiro, K.; Mizusaki, J. Thermal and Chemical Lattice Expansibility of $La_{0.6}Sr_{0.4}Co_{1-y}Fe_yO_{3-\delta}$ (Y = 0.2, 0.4, 0.6 and 0.8). *Solid State Ionics* **2011**, *186*, 37−43.
(20) Lein, H.; Wiik, K.; Grande, T. Thermal and Chemical Expansion of Mixed Conducting $La_{0.5}Sr_{0.5}Fe_{1-x}Co_xO_{3-\delta}$ Materials. *Solid State Ionics* **2006**, *177*, 1795−1798.
(21) Chen, Yu; Adler, S. B. Thermal and Chemical Expansion of Sr-Doped Lanthanum Cobalt Oxide ($La_{1-x}Sr_xCoO_{3-\delta}$). *Chem. Mater.* **2005**, *17*, 4537−4546.
(22) Boroomand, F.; Wessel, E.; Bausinger, H.; Hilpert, K. Correlation between Defect Chemistry and Expansion during Reduction of Doped $LaCrO_3$ Interconnects for SOFCs. *Solid State Ionics* **2000**, *129*, 251−258.
(23) Perry, N. H.; Bishop, S. R.; Tuller, H. L. Tailoring Chemical Expansion by Controlling Charge Localization: In Situ X-Ray Diffraction and Dilatometric Study of $(La,Sr)(Ga,Ni)O_{3-\delta}$ Perovskite. *J. Mater. Chem. A* **2014**, *2*, 18906−18916.
(24) Grande, T.; Tolchard, J. R.; Selbach, S. M. Anisotropic Thermal and Chemical Expansion in Sr-Substituted $LaMnO_{3+x}$: Implications for Chemical Strain Relaxation. *Chem. Mater.* **2012**, *24*, 338−345.
(25) Selbach, S. M.; Tybell, T.; Einarsrud, M.-A.; Grande, T. Structure and Properties of Multiferroic Oxygen Hyperstoichiometric $BiFe_{1-x}Mn_xO_{3+\delta}$. *Chem. Mater.* **2009**, *21*, 5176−5186.
(26) Selbach, S. M.; Tybell, T.; Einarsrud, M.-A.; Grande, T. High-Temperature Semiconducting Cubic Phase of $BiFe_{0.7}Mn_{0.3}O_{3+\delta}$. *Phys. Rev. B: Condens. Matter Mater. Phys.* **2009**, *79*, 214113.
(27) Chen, X.; Grande, T. Anisotropic Chemical Expansion of $La_{1-x}Sr_xCoO_{3-\delta}$. *Chem. Mater.* **2013**, *25*, 927−934.
(28) Chen, X.; Grande, T. Anisotropic and Nonlinear Thermal and Chemical Expansion of $La_{1-x}Sr_xFeO_{3-\delta}$(x = 0.3, 0.4, 0.5) Perovskite Materials. *Chem. Mater.* **2013**, *25*, 3296−3306.
(29) Tokura, Y.; Tomioka, Y. Colossal Magnetoresistive Manganites. *J. Magn. Magn. Mater.* **1999**, *200*, 1−23.
(30) Becher, C.; Maurel, L.; Aschauer, U.; Lilienblum, M.; Magén, C.; Meier, D.; Langenberg, E.; Trassin, M.; Blasco, J.; Krug, I. P.; et al. Strain-Induced Coupling of Electrical Polarization and Structural Defects in $SrMnO_3$ Films. *Nat. Nanotechnol.* **2015**, *10*, 661−665.
(31) Rondinelli, J. M.; Eidelson, A. S.; Spaldin, N. A. Non-d^0 Mn-Driven Ferroelectricity in Antiferromagnetic $BaMnO_3$. *Phys. Rev. B: Condens. Matter Mater. Phys.* **2009**, *79*, 205119.
(32) Günter, T.; Bousquet, E.; David, A.; Boullay, P.; Ghosez, P.; Prellier, W.; Fiebig, M. Incipient Ferroelectricity in 2.3% Tensile-Strained $CaMnO_3$ Films. *Phys. Rev. B: Condens. Matter Mater. Phys.* **2012**, *85*, 214120.
(33) Poeppelmeier, K. R.; Leonowicz, M. E.; Scanlon, J. C.; Longo, J. M.; Yelon, W. B. Structure Determination of $CaMnO_3$ and $CaMnO_{2.5}$ by X-Ray and Neutron Methods. *J. Solid State Chem.* **1982**, *45*, 71−79.
(34) Negas, T.; Roth, R. S. The System $SrMnO_{3-X}$. *J. Solid State Chem.* **1970**, *1*, 409−418.
(35) Zeng, Z.; Greenblatt, M.; Croft, M. Large Magnetoresistance in Antiferromagnetic $CaMnO_{3-X}$. *Phys. Rev. B: Condens. Matter Mater. Phys.* **1999**, *59*, 8784−8788.
(36) Sasaki, S.; Prewitt, C. T.; Bass, J. D.; Schulze, W. A. IUCr. Orthorhombic Perovskite $CaTiO_3$ and $CdTiO_3$: Structure and Space

Group. *Acta Crystallogr., Sect. C: Cryst. Struct. Commun.* **1987**, *43*, 1668−1674.
(37) Shirane, G.; Yamada, Y. Lattice-Dynamical Study of the 110 K Phase Transition in $SrTiO_3$. *Phys. Rev.* **1969**, *177*, 858−863.
(38) Hewat, A. W. Structure of Rhombohedral Ferroelectric Barium Titanate. *Ferroelectrics* **1973**, *6*, 215−218.
(39) Szot, K.; Speier, W.; Carius, R.; Zastrow, U.; Beyer, W. Localized Metallic Conductivity and Self-Healing during Thermal Reduction of $SrTiO_3$. *Phys. Rev. Lett.* **2002**, *88*, No. 075508.
(40) Koonce, C. S.; Cohen, M. L.; Schooley, J. F.; Hosler, W. R.; Pfeiffer, E. R. Superconducting Transition Temperatures of Semiconducting $SrTiO_3$. *Phys. Rev.* **1967**, *163*, 380−390.
(41) Kan, D.; Terashima, T.; Kanda, R.; Masuno, A.; Tanaka, K.; Chu, S.; Kan, H.; Ishizumi, A.; Kanemitsu, Y.; Shimakawa, Y.; et al. Blue-Light Emission at Room Temperature from Ar+-Irradiated $SrTiO_3$. *Nat. Mater.* **2005**, *4*, 816−819.
(42) Kolodiazhnyi, T.; Tachibana, M.; Kawaji, H.; Hwang, J.; Takayama-Muromachi, E. Persistence of Ferroelectricity in $BaTiO_3$ through the Insulator-Metal Transition. *Phys. Rev. Lett.* **2010**, *104*, 147602.
(43) Kresse, G.; Hafner, J. Ab Initio Molecular Dynamics for Liquid Metals. *Phys. Rev. B: Condens. Matter Mater. Phys.* **1993**, *47*, 558−561.
(44) Kresse, G.; Hafner, J. Ab Initio Molecular-Dynamics Simulation of the Liquid-Metal-Amorphous-Semiconductor Transition in Germanium. *Phys. Rev. B: Condens. Matter Mater. Phys.* **1994**, *49*, 14251−14269.
(45) Kresse, G.; Furthmüller, J. Efficient Iterative Schemes for Ab Initio Total-Energy Calculations Using a Plane-Wave Basis Set. *Phys. Rev. B: Condens. Matter Mater. Phys.* **1996**, *54*, 11169.
(46) Kresse, G.; Furthmüller, J. Efficiency of Ab-Initio Total Energy Calculations for Metals and Semiconductors Using a Plane-Wave Basis Set. *Comput. Mater. Sci.* **1996**, *6*, 15−50.
(47) Blöchl, P. E. Projector Augmented-Wave Method. *Phys. Rev. B: Condens. Matter Mater. Phys.* **1994**, *50*, 17953.
(48) Perdew, J. P.; Ruzsinszky, A.; Csonka, G. I.; Vydrov, O. A.; Scuseria, G. E.; Constantin, L. A.; Zhou, X.; Burke, K. Restoring the Density-Gradient Expansion for Exchange in Solids and Surfaces. *Phys. Rev. Lett.* **2008**, *100*, 136406.
(49) Koehler, W. C.; Wollan, E. O. Neutron-Diffraction Study of the Magnetic Properties of Perovskite-like Compounds LaBO3. *J. Phys. Chem. Solids* **1957**, *2*, 100−106.
(50) Takeda, T.; Ohara, S. Magnetic Structure of the Cubic Perovskite Type SrMnO3. *J. Phys. Soc. Jpn.* **1974**, *37*, 275.
(51) Rice, W. D.; Ambwani, P.; Bombeck, M.; Thompson, J. D.; Haugstad, G.; Leighton, C.; Crooker, S. A. Persistent Optically Induced Magnetism in Oxygen-Deficient Strontium Titanate. *Nat. Mater.* **2014**, *13*, 481−487.
(52) Anisimov, V. I.; Zaanen, J.; Andersen, O. K. Band Theory and Mott Insulators: Hubbard *U* Instead of Stoner. *Phys. Rev. B: Condens. Matter Mater. Phys.* **1991**, *44*, 943−954.
(53) Anisimov, V. I.; Aryasetiawan, F.; Lichtenstein, A. I. First-Principles Calculations of the Electronic Structure and Spectra of Strongly Correlated Systems: The **LDA** + *U* Method. *J. Phys.: Condens. Matter* **1997**, *9*, 767−808.
(54) Wang, L.; Maxisch, T.; Ceder, G. Oxidation Energies of Transition Metal Oxides within the GGA + *U* Framework. *Phys. Rev. B: Condens. Matter Mater. Phys.* **2006**, *73*, 195107.
(55) Becke, A. D. A New Mixing of Hartree−Fock and Local Density-functional Theories. *J. Chem. Phys.* **1993**, *98*, 1372−1377.
(56) Hong, J.; Stroppa, A.; Íñiguez, J.; Picozzi, S.; Vanderbilt, D. Spin-Phonon Coupling Effects in Transition-Metal Perovskites: A DFT + *U* and Hybrid-Functional Study. *Phys. Rev. B: Condens. Matter Mater. Phys.* **2012**, *85*, 54417.
(57) Santana, J. A.; Krogel, J. T.; Kent, P. R. C.; Reboredo, F. A. Diffusion Quantum Monte Carlo Calculations of SrFeO3 and LaFeO3. *J. Chem. Phys.* **2017**, *147*, No. 034701.
(58) Santana, J. A.; Mishra, R.; Krogel, J. T.; Borisevich, A. Y.; Kent, P. R. C.; Pantelides, S. T.; Reboredo, F. A. Quantum Many-Body Effects in Defective Transition-Metal-Oxide Superlattices. *J. Chem. Theory Comput.* **2017**, *13*, 5604−5609.
(59) Cuong, D. D.; Lee, B.; Choi, K. M.; Ahn, H.-S.; Han, S.; Lee, J. Oxygen Vacancy Clustering and Electron Localization in Oxygen-Deficient $SrTiO_3$: LDA + *U* Study. *Phys. Rev. Lett.* **2007**, *98*, 115503.
(60) Choi, M.; Oba, F.; Tanaka, I. Role of Ti Antisitelike Defects in $SrTiO_3$. *Phys. Rev. Lett.* **2009**, *103*, 185502.
(61) Choi, M.; Oba, F.; Kumagai, Y.; Tanaka, I. Anti-Ferrodistortive-Like Oxygen-Octahedron Rotation Induced by the Oxygen Vacancy in Cubic $SrTiO_3$. *Adv. Mater.* **2013**, *25*, 86−90.
(62) Hu, Z.; Metiu, H. Choice of *U* for DFT+ *U* Calculations for Titanium Oxides. *J. Phys. Chem. C* **2011**, *115*, 5841−5845.
(63) Dudarev, S. L.; Botton, G. A.; Savrasov, S. Y.; Humphreys, C. J.; Sutton, A. P. Electron-Energy-Loss Spectra and the Structural Stability of Nickel Oxide: An LSDA+*U* Study. *Phys. Rev. B: Condens. Matter Mater. Phys.* **1998**, *57*, 1505−1509.
(64) Shannon, R. D.; Prewitt, C. T. IUCr. Effective Ionic Radii in Oxides and Fluorides. *Acta Crystallogr., Sect. B: Struct. Crystallogr. Cryst. Chem.* **1969**, *25*, 925−946.
(65) Sasaki, S.; Prewitt, C. T.; Bass, J. D.; Schulze, W. A. IUCr. Orthorhombic Perovskite $CaTiO_3$ and $CdTiO_3$: Structure and Space Group. *Acta Crystallogr., Sect. C: Cryst. Struct. Commun.* **1987**, *43*, 1668−1674.
(66) Bader, R. F. W. A Quantum Theory of Molecular Structure and Its Applications. *Chem. Rev.* **1991**, *91*, 893−928.
(67) Goodenough, J. B. Perspective on Engineering Transition-Metal Oxides. *Chem. Mater.* **2014**, *26*, 820−829.
(68) Lin, C.; Demkov, A. A. Electron Correlation in Oxygen Vacancy in SrTiO3. *Phys. Rev. Lett.* **2013**, *111*, 217601.
(69) Carrasco, J.; Illas, F.; Lopez, N.; Kotomin, E. A.; Zhukovskii, Y. F.; Evarestov, R. A.; Mastrikov, Y. A.; Piskunov, S.; Maier, J. First-Principles Calculations of the Atomic and Electronic Structure of F Centers in the Bulk and on the (001) Surface of $SrTiO_3$. *Phys. Rev. B: Condens. Matter Mater. Phys.* **2006**, *73*, No. 064106.
(70) Curnan, M. T.; Kitchin, J. R. Effects of Concentration, Crystal Structure, Magnetism, and Electronic Structure Method on First-Principles Oxygen Vacancy Formation Energy Trends in Perovskites. *J. Phys. Chem. C* **2014**, *118*, 28776−28790.
(71) Bergerud, A.; Selbach, S. M.; Milliron, D. J. Oxygen Incorporation and Release in Metastable Bixbyite V_2O_3 Nanocrystals. *ACS Nano* **2016**, *10*, 6147−6155.
(72) Thomson, R.; Levine, L.; Stauffer, D. Theory of Strain Percolation in Metals: Mean Field and Strong Boundary Universality Class. *Phys. A* **2000**, *283*, 307−327.
(73) Das, T.; Nicholas, J. D.; Qi, Y. Polaron Size and Shape Effects on Oxygen Vacancy Interactions in Lanthanum Strontium Ferrite. *J. Mater. Chem. A* **2017**, *5*, 25031.

https://dx.doi.org/10.1021/acs.jpcc.0c02060
J. Phys. Chem. C 2020, 124, 12922−12932